A Joint DFT-kMC Study to Model Ethylene Carbonate Decomposition Reactions : SEI Formation, Growth, and Capacity Loss During Calendar aging of Li-Metal Batteries

Mohammed Bin Jassar, Carine Michel, Sara Abada, Theodorus de Bruin, Sylvain Tant, Carlos Nieto-Draghi, Stephan Steinmann

To cite this version:

Mohammed Bin Jassar, Carine Michel, Sara Abada, Theodorus de Bruin, Sylvain Tant, et al.. A Joint DFT-kMC Study to Model Ethylene Carbonate Decomposition Reactions : SEI Formation, Growth, and Capacity Loss During Calendar aging of Li-Metal Batteries. ACS Applied Energy Materials, 2023, 6 (13), pp.6934-6945. 10.1021/acsaem.3c00372 . hal-04172957

HAL Id: hal-04172957

https://ifp.hal.science/hal-04172957v1

Submitted on 28 Jul 2023

A joint DFT-kMC study to model ethylene carbonate decomposition reactions: SEI formation, growth, and capacity loss during calendar aging of Li-metal batteries

Mohammed Bin Jassar,[1,2,3] Carine Michel,[2] Sara Abada,[4] Theodorus De Bruin,[3] Sylvain Tant,[1] Carlos Nieto-Draghi,[3] and Stephan N. Steinmann[2*]*

[1]Stellantis - Centre Technique de Carrière-sous-Poissy, 212 Boulevard Pelletier 78955 Carrière-sous-Poissy, France

[2]ENS de Lyon, CNRS, Laboratoire de Chimie UMR 5182, 69364 Lyon, France

[3] IFP Energies nouvelles, 1 et 4 avenue de Bois-Préau, 92852 Rueil-Malmaison, France

[4] IFP Energies nouvelles, Rond-Point de L'échangeur de Solaize—BP3, 69360 Solaize, France

Corresponding Authors

* E-mail: carlos.nieto@ifpen.fr ; stephan.steinmann@ens-lyon.fr

Abstract

The solid electrolyte interphase (SEI) is a multi-structured thin layer that forms at the anode (e.g., lithium-metal)/electrolyte (e.g., ethylene carbonate EC) interface due to electrolyte reduction. At the initial battery cycles, the SEI protects the electrolyte from further reduction. However, the SEI continues to grow with time leading to capacity loss and eventually the death of the battery. In this work, we modeled the battery-aging process at storage conditions (calendar aging). We studied EC decomposition reactions using density functional theory (DFT) simulations in the gas-phase in isolation and over the inorganic layer found inside the SEI composed of Li_2CO_3. We used the values obtained from DFT alongside diffusion coefficients from the literature to explore the temporal evolution of the concentration of species by kinetic Monte Carlo (kMC) simulations. We found that reactions occurring over Li_2CO_3 (001) led to a relatively slow SEI growth which is compatible with the general use of carbonate-based solvents in LIBs for protection/passivation purposes. Our simulations over Li_2CO_3 (001) predict the formation of a multilayered structured SEI. Moreover, our kMC simulations predict the shift from a non-linear initial behavior to a linear behavior for the capacity loss induced by the formation and growth of the SEI over time which was reported in previous experimental and theoretical studies for lithiated graphite-based batteries. We extended our analysis to the decomposition reactions over the Li_2O (111) surface which could form from the decomposition of Li_2CO_3. We found that the selectivity of the decomposition reactions strongly depends on the inorganic surface. The main conclusion of this study is to highlight the crucial role played by surface reactions inside the SEI on the nature and selectivity of the decomposition kinetics of EC for the SEI growth.

Keywords: lithium-metal battery, solid electrolyte interphase, density functional theory, kinetic Monte Carlo simulation, calendar aging

1. Introduction

Batteries have been used and undergone continual improvement to meet market requirements and enhance daily life’s activities[1,2]. Among the various battery types, lithium-ion batteries (LIBs) are playing an increasingly important role in energy storage due to their high-power density, high energy density, low self-discharge and low reduction potential of Li (−3.04 V with respect to the standard hydrogen electrode)[1]. However, the performance of the battery tends to deteriorate over time due to irreversible chemical processes that take place[3–5]. This gradual deterioration of the battery is governed by a process called battery-aging which can be cyclic (when the battery is used) or calendar (i.e., even if the battery is stored) [3–5]. The complex aging mechanisms can be categorized into loss of active and accessible electrode material (LAM), loss of Li inventory (LLI) and loss of conductivity (CL) in the electrode[6]. LLI is considered to be the primary aging mechanism leading to capacity loss. LLI mainly arises from the formation and growth of a thin layer (nanometer in thickness) at the anode/electrolyte interface called the solid electrolyte interphase (SEI)[7,8]. The SEI forms due to the reduction of the electrolyte by electrons from the anode[7]. The formation of the passivating SEI at the initial cycles of the battery usage protects the electrolyte from further reduction. However, the SEI layer continues to grow over time consuming further electrons and electrolyte leading to capacity loss and eventually the death of the battery[1,7].

The SEI is viewed as a heterogeneous multilayered structure: an inner inorganic layer near the anode/SEI interface and an outer organic layer close to the SEI/electrolyte interface[7,9,10]. The nature of the anode and the electrolyte used affects the composition and the structure of the SEI layer[1,7,8]. Materials such as graphite Li-metal, silicon and tin have been used as anode materials[1,7,8]. The electrolyte used is generally composed of organic solvents, salts, and additives[1,7,8]. The commonly used solvent in LIBs is a mixture of cyclic carbonates like ethylene carbonate (EC) and linear carbonates: dimethyl carbonate (DMC), diethyl carbonate (DEC) or/and ethyl methyl carbonate (EMC). Most studies have been focusing on the cyclic EC which is the main solvent as it forms a stable SEI when it decomposes[1,7,8]. EC was found to have a higher electron affinity than linear carbonates (DMC, DEC, EMC), which makes EC most prone to reduction in cyclic/linear mixed electrolytes[7].

For the SEI formed in EC-based electrolytes, experimental studies evidenced the presence of various species like Li_2CO_3 and alkyl carbonate $(ROCO_2Li)_2$ representing the inorganic and organic species respectively[1,7–12]. The alkyl carbonate species formed inside the SEI are generally dilithium butylene dicarbonate (Li_2BDC) and dilithium ethylene dicarbonate (Li_2EDC). Even though experimental studies were able to give us an idea about the composition of the SEI, other aspects like thermodynamics and kinetics of the SEI formation and growth are hard to investigate due to the limitation of experimental techniques[1,7,8]. Theoretical studies have been performed to understand the thermodynamics, kinetics and composition of the SEI layer[7,8,13–19]. Previous theoretical studies (e.g., DFT-based) have been used to model the very initial steps of EC reduction reactions by lithium radicals (Li^0) in isolation, (“only” Li^0 and EC, as initial reactants) or Li-metal[13,14,20–22]. It was proposed that the decomposition reactions forming the SEI starts once Li^0 attacks EC, forming the closed Li-EC complex cLi-EC• (c stand for closed and • to indicate that the species is a radical). cLi-EC• undergoes a ring-opening reaction leading to oLi-EC• (o stands for opened) which in turn initiates a cascade of reactions to form Li_2CO_3 and/or $(ROCO_2Li)_2$[7,8,13–18]. Since DFT-based methods are restricted to very short time scales, they are only directly applicable to the fast initiation reactions but cannot model the long-time evolution of large systems, characteristic for the slow growth of the SEI.

Continuum models can extend the simulation time and help to understand battery-aging processes that cannot be obtained by DFT[7,8,23,24]. Christensen et al. developed a continuum model of the SEI growth, assuming the SEI is mainly composed of Li_2CO_3[25]. They found that the SEI growth inducing capacity loss is faster for charged batteries where the anode contains more (reactive) electrons than for uncharged batteries[25]. Another continuum model developed by Kolzenberg et al. predicted a shift from an initial non-linear behavior of SEI growth with time to a linear regime at the long-term[26]. A shift to linear capacity loss was also observed experimentally by different groups during cyclic and calendar aging[3,5,27–29]. Such continuum models can extend the simulation time, but they do not provide us with molecular and structural insights on the kinetics of the capacity loss induced by SEI growth[7].

Kinetic Monte Carlo (kMC)-based models have attracted interest since they can simulate longer time scales (from milliseconds to hours) compared to what is attainable in DFT (picoseconds) and molecular dynamics MD (10^{-9}–10^{-6}s)[30]. Still, kMC explicitly describes the geometric evolution of a given system via stochastic reaction sequences and, thus, gives more structural insights than continuum models[30]. kMC uses a library of rate constants of elementary chemical reactions that are obtained from experiments or atomistic models (e.g., DFT)[8,30]. Previous kMC models employed in electrochemical systems like fuel cells, Li-O_2 batteries and slurry redox flow batteries used on-lattice structural models[31]. In this common setup, species (atoms or molecules) occupy one or more discrete lattice sites[30]. Such kMC models can model reactions and diffusion events. For example, Thangavel et al. developed a kMC model for simulating the evolution of the carbon/sulfur mesostructure for discharging Li-S batteries where the rate constants of the electrochemical reactions were calculated using Butler Volmer type equations[31]. Another kMC model developed by Yin et al. simulated the process of Li_2O_2 thin film growth during discharging of Li-O_2 batteries[32]. They found that Li_2O_2 thin layer ordering is determined by the interplay between reaction and diffusion kinetics. In the context of the SEI in LIBs, previous kMC models were used to study the effect of some parameters like temperature and the charging rate on the charging time and SEI thickness[8]. A more detailed study by Abbott et al. performed DFT calculation in the gas-phase in isolation for EC decomposition reactions and used the values to perform a kinetically corrected Monte Carlo−Molecular Dynamics simulations to study the SEI growth. Their model predicts a multilayered structure of the SEI. Furthermore, the simulations reveal the onset of Li_2CO_3 crystallization[15] in agreement with an experimental study where Li_2CO_3 crystallites were observed in the SEI[33]. A recent study by Spotte-Smith et al.[17] performed DFT calculations for EC decomposition reactions also in the gas-phase in isolation to obtain their corresponding energy barriers (E_b). They used the DFT values to obtain the rate constants of each reaction to be used in a 1D kMC model to study the SEI growth at different values of electrostatic potential. They also predicted a multilayered structure SEI[17].

Previous joint DFT-kMC studies were able to predict a plausible SEI structure but none of them reported the way the capacity loss induced by the SEI growth evolves with time. In addition, previous DFT methods used to study EC decomposition reactions were considering the decomposition reactions in isolation or Li-metal[13,14,17,20–22]. However, once the SEI layer is formed, the electrode is in contact with a series of layers from an inner inorganic layer to an outer organic layer which is in contact with the electrolyte (anode/inorganic-layer/organic-layer/electrolyte)[7–10]. Single et al. were the first to suggest that SEI growth reaction happens inside the SEI but did not specify the exact interface where the decomposition reactions occur[34]. The organic layer is a composite heterogeneous and porous material allowing the transport of EC molecules[2,7]. Since Li^0 will immediately react with the reducible organic species, it cannot diffuse through the organic layer of SEI. The inorganic layer is dense and permeable to Li^0/Li^+ but not to the much larger EC molecules[7,35]. It should be noted that the Li^0 diffusion inside the inorganic SEI was first proposed by Shi et al.[35]. After that, follow-up studies by different groups investigated the effect of Li^0 diffusion on the SEI growth and capacity loss[23,26]. They suggest that Li^0 is the most likely electron transport mechanism for the SEI growth and predicted a shift to linear SEI growth with time[23,26]. Hence, we expect the SEI growth reactions to occur over the inorganic layer (e.g., Li_2CO_3) at the inorganic/organic (in/organic) interface inside the SEI, see Figure 1, i.e., by solvent diffusion from the electrolyte through the porous structure of the organic layer, until the solvent molecule reaches the dense inorganic layer, where it reacts with Li^0 that has diffused from the electrode to the in/organic interface.

Note that in commercial batteries the electrolyte is very complex and contains many species including salts (e.g., $LiPF_6$) and additives (e.g., VC). $LiPF_6$ and VC are added to the electrolyte to enhance some electrolyte properties like ionic conductivity and temperature range[1,7,8]. They contribute to the SEI structure and composition. For example, the decomposition of $LiPF_6$ lead to the formation of LiF which was reported to be present the in SEI[1,7,8,28,36,37]. However, studying the decomposition reactions of realistic electrolyte mixture including their corresponding decomposition pathways is very challenging and computational too expensive. Considering this limitation, in this work, we focus on studying the SEI formation and growth during calendar aging of an LIB using a model system containing Li-metal as the anode and EC as the solvent. It is important to mention that the main consequence of not including other electrolyte species (e.g., $LiPF_6$ and VC) in our study is probably the oversimplification of the heterogeneous SEI formed in our simulations compared with the one observed in real batteries. In that context, our work can be considered as an approach to the formation of SEI using a simplified electrolyte composition. We perform DFT calculations for the set of EC decomposition reactions commonly discussed in the literature. For reference purposes, we study the reactions in the isolated gas-phase similar to previous studies and inside the SEI layer. Our main aim is to analyze the reactions over the inorganic layer of Li_2CO_3 and assess the effect of the surface (i.e., SEI) on the thermodynamics and kinetics of these decomposition reactions. We mainly focus on the cLi-EC• ring-opening reaction that starts the whole cascade of reactions. For this purpose, we used a slab of Li_2CO_3 (001) as can be seen in Figure S1, which corresponds to the most stable and most abundant, surface orientation of Li_2CO_3 and hence is most likely formed in the SEI[38]. Then, we used the activation energies and rate constants obtained from DFT calculations alongside diffusion coefficients from literature[38–40] in a kMC model to study the growth of the SEI layer (composition and kinetics) and the capacity loss with time. It should be noted that, since we are modeling calendar aging of the battery, all the DFT and kMC calculations were performed in the absence of any electric field to mimic an inactive battery (at storage conditions).

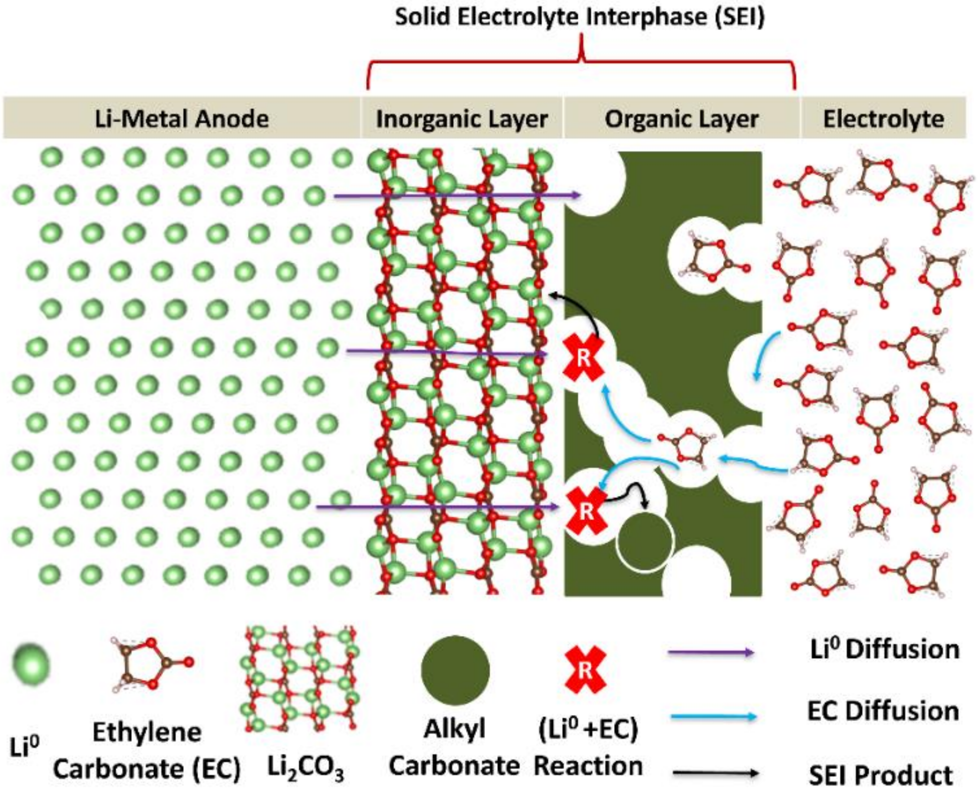

Figure 1: The interface where SEI growth reactions are expected to occur.

2. Methods and Computational Details

2.1 DFT Computational Details

All DFT calculations have been performed using the Vienna Ab initio Simulation Package VASP 5.4.4.[41–44] using the Perdew−Burke−Ernzerhof functional (GGA-PBE)[45]. Dispersion interactions were included using the density-dependent dispersion correction dDsC[46,47]. The projector augmented plane-wave (PAW) pseudopotential was used to describe the core electrons. All structures were optimized using the conjugate gradient algorithm in the gas-phase in isolation (no slab) and over the slab of Li_2CO_3 (001), where (001) is the most stable surface orientation of Li_2CO_3[38]. The slab used to model Li_2CO_3 (001) layer is made of four layers, see Figure S1, where the bottom two are fixed. 12 Å of vacuum spacing were introduced to reduce the periodic interaction in the direction normal to the slab. The k-point sampling of the first Brillouin zone was performed with a $1 \times 1 \times 1$ Monkhorst–Pack[48] grid for the isolated molecules, $3 \times 3 \times 1$ grid for the slab Li_2CO_3 (001) calculations and $5 \times 5 \times 5$ grid for bulk Li_2CO_3 calculations. Convergence criteria for the calculations were set to 10^{-6} eV and 0.03 eV/Å, for the electronic self-consistency iterations and ionic relaxation loop respectively. A Fermi smearing with a width of 0.03 eV was employed. Spin polarized calculations are performed for radical species (such as cLi-EC•). The cutoff energy for the plane-wave-basis was set to 600 eV. Since we are interested in modeling the battery during calendar aging, i.e., the battery is inactive, we did not apply an electrochemical potential.

To obtain the energy barriers (E_b), the optimized geometries of reactants and products were used as inputs for the Opt'n Path software[49] to have a rough estimate of the minimum energy path (MEP) connecting them. The Nudged Elastic Band method (NEB)[50] was used to find a more accurate MEP and a possible transition state (TS) structure by creating 8 images between the initial and final states. Once the potential candidate for a TS was identified, the dimer method[51] was exploited to optimize the possible TS geometry. Finally, to ensure the nature of the potential candidate as a TS, a vibrational frequency calculation was performed. In the case of a TS, only one imaginary frequency should be obtained, which corresponds to the chemical reaction of interest.

2.2 Kinetic Monet Carlo (kMC)

Monte Carlo (MC) methods are computational algorithms that help obtain numerical results by random sampling[52–54]. In the present work, we have used the classical kMC method, usually named the “n-fold way”, in the framework of the Bortz, Kalos, and Lebowitz (BKL) approach[52–54]. Our kMC simulations were performed using SPPARKS software which is a parallel MC code[55]. We have adapted the on-lattice application “erbium” of SPPARKS to our system to include enough species to model the growth of our SEI model. More details about the kMC methodology and code modifications are found in the supporting information. Any event (reaction/diffusion) to occur in the “erbium” application must be described by an energy barrier/rate constant. If “two” species are meant to react to form “one” new species, they have to meet in space and a vacant site would be added to conserve the initial number of sites, Eq. (1).

$$\mathrm{A} + \mathrm{B} \ \rightarrow \mathrm{C} + \text{vacant site} \qquad (1)$$

For the SEI to grow, three main factors are important: Li^0 diffusion, EC diffusion and decomposition reactions’ energy barriers. In our simulation, all chemical reactions are considered reversible. SPPARKS also allows for calculation of diffusion coefficients. Additional details on the kMC parameters and the validation of the diffusion coefficient obtained through the mean square displacement are provided in the supporting information.

kMC set-up

The on-lattice kMC application implemented in the work represents a constant volume system, which has important implications in the way the reaction paths are considered. In practice, to avoid dilution of the system due to the production of gases, we assumed that once a gas molecule forms (e.g., C_2H_4), see Eq. (2), it immediately escapes from the volume control of our kMC simulations close to the SEI layer through combination of Eq. (2) and Eq. (3) to give Eq. (4):

$$\mathrm{A} + \mathrm{B} \rightarrow \mathrm{C} + \mathrm{C_2H_4} \tag{2}$$

$$\mathrm{C_2H_4} \rightarrow \text{vacant site} \tag{3}$$

$$\mathrm{A} + \mathrm{B} \rightarrow \mathrm{C} + \text{vacant site} \tag{4}$$

The concentration of any species (e.g., i), $[\mathrm{C_i}]$, is calculated using:

$$[\mathrm{C_i}] = \frac{\mathrm{N_i}}{\mathrm{N_A V_{total}}} \tag{5}$$

, where $\mathrm{N_i}$ is the number of species i inside the simulation box, $\mathrm{N_A}$ is Avogadro's number and $\mathrm{V_{total}}$ is the total volume of the simulation box.

The initial conditions of our kMC simulation where the solvent (EC) is in direct contact with the Li-metal, see Figure S6. We used a simulation box with dimensions 8.8 nm × 8.8 nm × 35.2 nm corresponding to a total volume of ≈ 2700 $\mathrm{nm^3}$. The total number of sites is 128000. The box is periodic in the plane (x and y) direction only. We used an FCC lattice to model our system. The FCC lattice constant (a) is set to be 4.4 Å, providing a molar volume of 13.0 $\mathrm{cm^3}$ $\mathrm{mol^{-1}}$ and specific capacity of around 3862 $\mathrm{mAh.g^{-1}}$ representing pure Li-metal anode as reported in the literature[1]. It should be noted that the local concentration of species (e.g., $\mathrm{Li^0}$) is calculated with respect to the volume occupied by that species. Around 4.4 nm (in z direction) of the simulation box is filled with $\mathrm{Li^0}$ with initial local concentration of $\left[\mathrm{C_{local\_Li^0}}\right]$ = 78.0 mol/l to mimic a Li-metal. Since we are using constant volume kMC (with the inherent fixed fcc-lattice size limitations) and to avoid EC being the limiting reactant (due to the lack of reducible species), the size of the EC compartment was set to be larger (around 30.8 nm in z direction, after the Li-metal zone) than that of the Li-metal with local concentration of that of the bulk liquid EC $[C_{\text{bulk\_EC}}] = [C_{\text{local\_EC}}] = 15.0$ mol/l in agreement with experimental values[1]. It should be noted that our on-lattice kMC setup is to be understood as a molecular kMC approach, i.e., lattice sites can host molecules, not just atoms. This implies that the volume occupied by a single molecule is not realistic (the lattice distance was chosen to be representative of metallic Li). However, to have realistic starting concentrations of the solvent (EC) we spaced the EC molecules with empty sites and since they are freely diffusing (no lateral interactions), the average concentration is then physically relevant. For sake of simplicity, we will be referring to the concentration of species with respect to the total volume of the simulation box following Eq. (5): $[C_{\text{EC}}] = 12.8$ mol/l and $[C_{\text{Li}^0}] = 9.7$ mol/l in the rest of the article. It should be noted that all species included in our model are neutral (e.g., Li^0, EC). All our kMC simulations have been performed at constant temperature of 298 K (25 °C), representing normal storage conditions at room temperature in the absence of an electrical current.

As discussed before, the inorganic species Li_2CO_3 is permeable to Li^0 but not to EC. In our model, on one hand, EC can diffuse through vacancies and the newly formed species (excluding Li_2CO_3) and is assumed to have diffusion constant in the bulk of $D_{\text{EC\_Bulk}} = 10^{-10}$ m^{2}s^{-1} and inside the organic SEI of $D_{\text{EC\_SEI}} = 10^{-13}$ m^{2}s^{-1} respectively as reported in previous studies[25,34,39,40,56]. On the other hand, Li^0 can diffuse only through the inorganic species Li_2CO_3. The diffusion coefficient of Li^0 inside the bulk Li_2CO_3 is assumed to be $D_{\text{Li}} = 10^{-14}$ m^{2}s^{-1} which falls in the range of Li diffusion inside the SEI as reported in the literature[34,38,57,58].

Note that several theoretical studies devoted to the transport of species in the solid phase usually use grain boundary models to calculate the diffusion coefficients. Hence, they intrinsically assume faster kinetics since diffusive species are placed close to solid edges. However, once the bulk structure of the crystal forms (as in the case of SEI growth), the "average" diffusion of species through the bulk solid phase will probably be slower. This inherent assumption affects the resulting time scale of kMC simulations, since both reactive and diffusion events are coupled in our model. The timescale in all our simulations must be considered as qualitative since it is difficult to link to any "real time" observed in experiments. More details about kMC methodology and assumptions made are found in the supporting information.

In all our calculations, we used the "tree" solver implemented in SPPARKS. Performance tests to check the effect of the number of cores on the results of simulations were made. It was found that the results are independent on the number of CPU cores used. Consequently, all calculations in the following sections were performed using 32 cores. All parameters used in SPPARKS, performance test and additional results are provided in the supporting information.

3. Results and Discussions

In the first subsection, we describe our DFT results for EC decomposition reactions in isolation and over Li_2CO_3 (001). In the second subsection, we discuss the kMC simulations' results for the SEI growth and capacity loss.

3.1 DFT

EC Decomposition Reactions in the Gas-Phase Isolation

The SEI starts to form when EC and Li^0 meet at the anode/electrolyte interface. Scheme 1 shows all decomposition reactions included in our study with energy values referring to the gas-phase. EC and Li^0 combine to form cLi-EC•, where the electron is located at the carbonyl carbon, which undergoes ring-opening reaction (R_I, where "R" stands for Reaction and "I" is the reaction number) to form oLi-EC• through an energy barrier of 23 kJ/mol. The electron is located at the terminal CH_2 of the newly formed product which could dissociate to ethylene (C_2H_4) and carbonate radical $LiCO_3$• (R_{II}) intermediate complex (through an energy barrier of 65 kJ/mol) where the electron is located at the oxygen (not connected to Li).

Once oLi-EC• is formed, a series of cascade reactions can occur. oLi-EC• can react with Li^0 to form Li_2CO_3 and C_2H_4 (R_{III}) or undergo coupling reaction with itself forming the alkyl carbonate Li_2BDC (R_{IV}) or it reacts with a carbonate radical $LiCO_3$• forming the other alkyl carbonate Li_2EDC (R_V) via a substitution reaction. $LiCO_3$• can also react with Li^0 to form Li_2CO_3 (R_{VI}). The barrierless formation of the carbonate and alkyl carbonate (Li_2BDC and Li_2EDC) has also been suggested in the literature[13–15]. It should be noted that all reactions obtained in the gas phase in isolation are exothermic except R_{II}, see supporting information for additional results and more details.

The inorganic part of the SEI layer (Li_2CO_3) forms through two paths (R_{III} and R_{VI}). We would expect more inorganic layer at high Li^0 concentration mostly through R_{III} since the energy barrier of R_{II} is the highest, and this reaction is essential for R_{VI} to occur. Away from the anode and closer to the electrolyte, Li^0 concentration decreases, and more organic species are expected[1,2,8,11,12,15]. The formations of the organic species Li_2BDC and Li_2EDC are barrierless but the decomposition of oLi-EC• (R_{II}) is required first for Li_2EDC. Consequently, based on the gas-phase DFT computations, we would expect Li_2BDC to form before Li_2EDC formation.

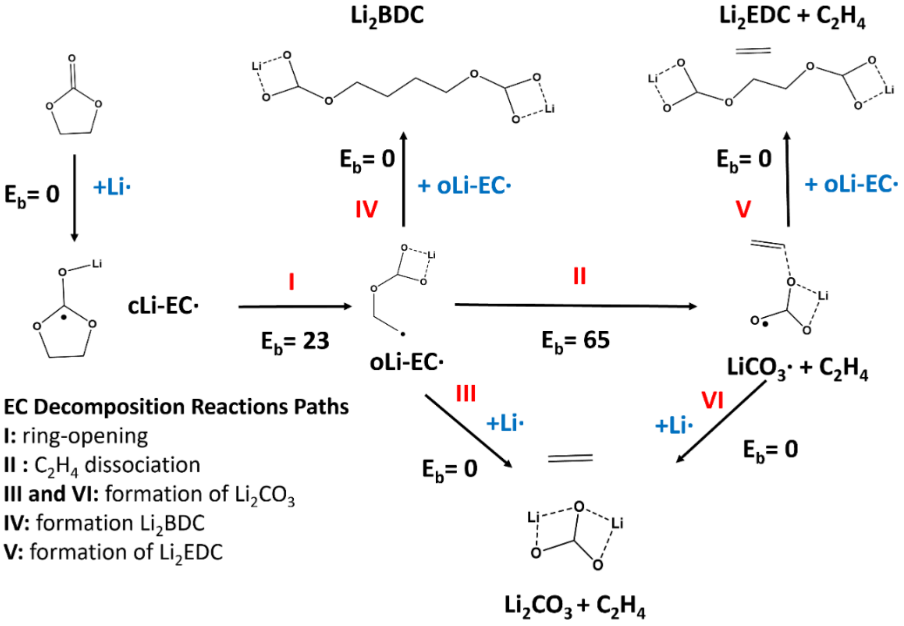

Scheme 1: Ethylene carbonate (EC) decomposition reactions in the gas-phase in isolation. E_b is the energy barrier of each reaction in kJ/mol.

EC Decomposition Reactions over Li_2CO_3 (001)

The diffusion of EC is faster than Li^0, see Section "kMC set-up". Hence, the decomposition reactions over the surface start with the adsorption of EC over the surface (S-EC) until it meets Li^0 diffusing through Li_2CO_3 coming from the anode to form S-cLi-EC•, where S stands for the surface Li_2CO_3 (001). Therefore, we have also investigated the reaction sequence on the most stable surface of Li_2CO_3. The relative energies of species over Li_2CO_3 (001) are shown in Figure 2. Even though most of the reactions over Li_2CO_3 (001) follow the same chemistry as in the gas-phase in isolation, we notice some differences in energy barriers and reaction energies for R_I and R_{II}. The surface stabilizes the species compared to the gas-phase case in isolation. For example, the effect of Li_2CO_3 (001) stabilize cLi-EC• leading to an increase in the energy barrier for ring-opening reaction R_I which initiates the cascade reactions. Consequently, it is harder to initiate the cascade reactions over Li_2CO_3 (001) since cLi-EC• is more stable in comparison with the isolation case. The transition state configuration for the ring-opening reaction over Li_2CO_3 (001) is shown in Figure 3. We notice that a Li atom of the surface is strongly interacting with the adsorbate. In contrast, the surface does not have a significant impact on the energy barrier of R_{II}. Additional results including the geometries of species over Li_2CO_3 (001) are found in the supporting information.

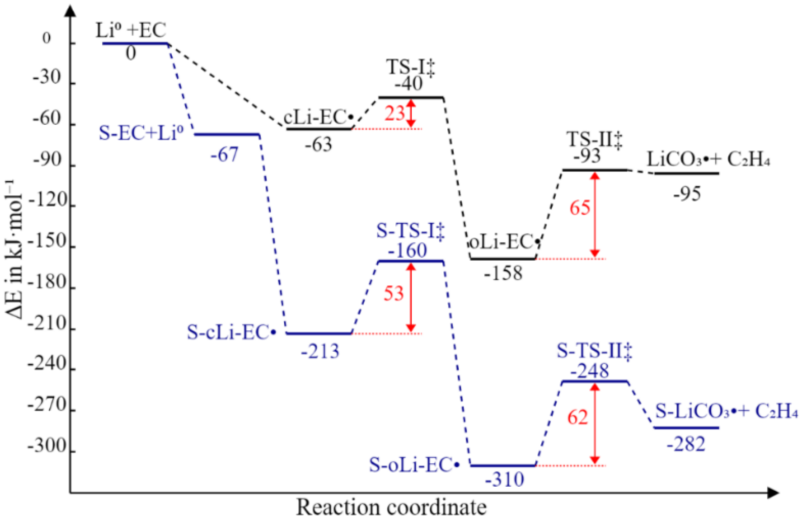

Figure 2 : EC decomposition reactions in isolation (black) and over Li_2CO_3 (001) (blue). S stands for surface.

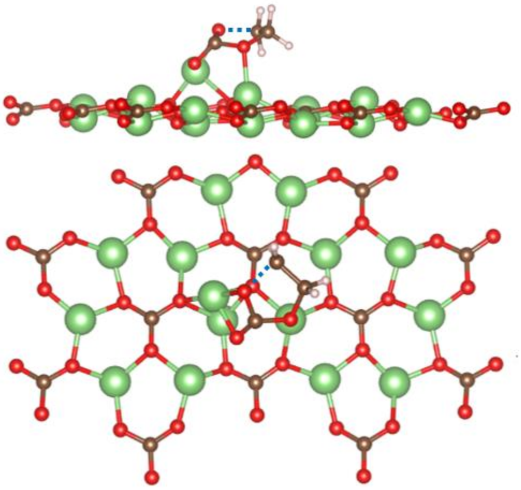

Figure 3: Side and top views of transition state geometry of the ring-opening reaction (R_I) over Li_2CO_3 (001). The colors: red, white, brown, and green represents oxygen, hydrogen, carbon, and lithium respectively. The blue dashed line represents the C-O bond distance (1.73 Å). Only the top layer of the surface in contact with reactive species is shown.

All barrierless reactions in Scheme 1 were found to be also barrierless over Li_2CO_3 (001) except for R_{IV}. This can be attributed, on one hand, to the fact that in the direct reaction of the two o-LiEC• to form Li_2BDC (in isolation), the reorientation to meet the "good" reaction configuration for C-C coupling reaction should come at no-cost. On the other hand, the surface stabilizes oLi-EC• leading to a C-C coupling with 13 kJ/mol energy barrier. In contrast, the oxygen radical in $LiCO_3$• is highly reactive, and undergoes reactions R_V and R_{VI} with no energy barrier even over Li_2CO_3 (001).

The energy barriers obtained from our calculations agree with those of a previous study by Zhang et al.[14]. However, it should be noted that the energy barriers vary in the literature and are sensitive to the level of theory used. Spotte-Smith et al.[17] reported that the energy barrier varies for EC decomposition reactions and gave an example for the cLi-EC• ring-opening reaction where the difference could reach 90 kJ/mol at different levels of theory. Herein, we target the difference between reactions in isolation and over the surfaces by keeping the same level of theory and assume that this relative quantity is more robust with respect to the level of theory.

To study the kinetics of the SEI growth over time considering the effect of diffusion of species, we used the obtained energy barriers to calculate the rate constants needed for our kMC model, see supporting information for details. In particular, kMC allows us to compare the relative effect of reactions occurring over Li_2CO_3 (001) with respect to the gas-phase case in isolation and the ensuing consequences on the kinetics and composition of the SEI growth and capacity loss.

3.2 kMC Results: Evolution of the SEI layer and Capacity Loss

EC Decomposition Reactions in the Gas-Phase in Isolation

Table S3 shows the physical parameters used in the kMC simulations. The initial configuration at time = 0 s before any SEI is formed and the concentration profile of species with time are shown in Figure 4a and 4b respectively. We notice the formation of SEI species: inorganic and organic species (Li_2CO_3 and alkyl carbonate (only Li_2BDC)) respectively with time in agreement to previous theoretical and experimental studies that predict their formation. The final concentration of Li_2CO_3 is around 5 times higher than the alkyl carbonates Li_2BDC. The small energy barrier for the ring-opening reaction (R_I) and the high concentration of Li^0 leads to the higher concentration of Li_2CO_3 since most reactions follow R_{III}. The lifetime for the oLi-EC• is short since it reacts immediately with Li^0 before it reacts with another oLi-EC• or $LiCO_3$• to form the alkyl carbonates. This explains the rapid consumption of Li^0 compared to EC: two Li^0 are consumed to form one Li_2CO_3 while only one EC is consumed. All Li_2CO_3 molecules formed were through R_{III} and not R_{VI}. This is due to the relatively high barrier of oLi-EC• decomposition (R_{II}) which is essential for (R_V) and (R_{VI}). This also explains the zero concentration observed for Li_2EDC. Our results agree with a previous ReaxFF MD study performed by Bedrov et al. that predicted the exclusive formation of Li_2BDC as the only alkyl carbonate formed from EC decomposition reactions in the gas-phase in isolation[59].

It should be noted that all intermediate radical species (cLi-EC•, oLi-EC• and $LiCO_3$•) have almost zero concentration throughout the simulation since they immediately react once they form. It is important to mention that the total concentration of C_2H_4 produced during the SEI formation assumed to escape from the system as defined in Eqs. (2) to (4) is 4.2 mol/l. The initial and final concentrations of all species in our kMC simulations are shown in Table S5.

The variation of the specific mass density profile along the Z-axis and a snapshot of the simulation box after all Li^0 have reacted after 0.6 microseconds (μs) for the gas-phase in isolation are shown in Figure 4c and 4d respectively. We notice the beginning of the formation of a dense layer: close to the Li-metal anode where the total density is principally determined by Li_2CO_3 and a few Li_2BDC molecules. This behavior agrees with what is expected from previous studies in the literature where the dense layer of the SEI is generally composed of inorganic species formed close to the anode[2,7,8].

We would like to mention that our simulations do not include the effect of quantum tunneling. This phenomenon is more important for the decomposition reactions at the very initial moments of SEI formation. Consequently, we can expect that the time scales reported in our simulations for the case of reaction in isolation are probably overestimated (i.e., quantum tunneling would probably slightly reduce the magnitude of the activation barriers). However, once the SEI starts to form the probability of quantum tunneling decreases and the reactions follow the trend observed in our simulations.

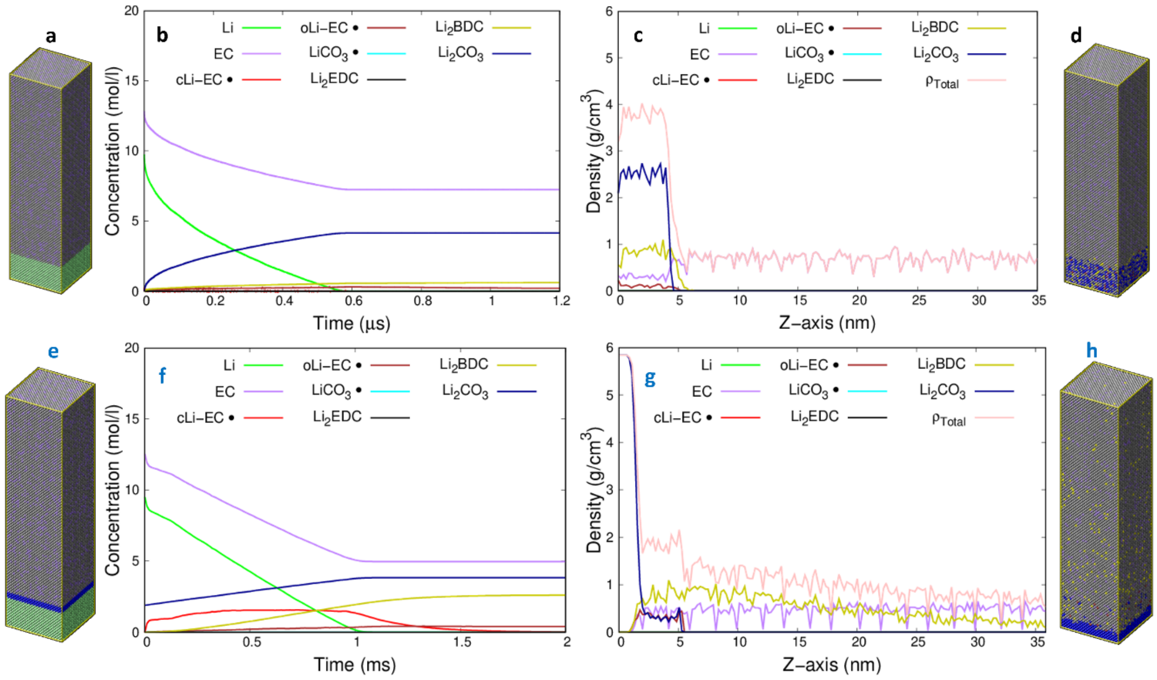

Figure 4: Summary of kMC results. a-d) Information of the EC decomposition reactions in isolation: a) Initial conditions b) Variation of the concentration of species vs. time c) Specific mass density profile along the Z-axis of the simulation box d) Snapshots of the simulation box after 0.6 µs. e-h) Information of the EC decomposition reactions over Li_2CO_3 (001): e) Initial

conditions f) Variation of the concentration of species vs. time g) Specific mass density profile along the Z-axis of the simulation box h) Snapshots of the simulation box after 1.2 ms. ρ_{total} is the total density.

EC Decomposition Reactions over Li_2CO_3 (001) and SEI growth

Following our assumption that the growth reactions take place over the inorganic layer inside the SEI, we performed kMC simulations using the configuration shown in Figure 4e where 4 layers of Li_2CO_3 (representing a concentration of 1.9 mol/l and 0.88 nm thickness in z direction) are placed between the EC and Li^0 compartments to mimic the influence of a preformed inorganic layer of the SEI. We used a slightly bigger simulation box with 8.8 nm × 8.8 nm× 36.08 nm to add the layers of Li_2CO_3 while maintaining the same initial local concentration of Li^0 and EC molecules as used in the study of the system at the gas-phase in isolation. The structure of the organic layer was neglected in the initial configuration since from our results in isolation, we notice the formations of small amounts of Li_2BDC compared to Li_2CO_3. In addition, since the precise structure of the organic layer is not known experimentally[2,7,8,12], we would like to avoid any assumption on the structure of the organic part of the SEI. In any case, our approximate rate constants do not depend on the organic layer. Over Li_2CO_3 (001), the movement of reactant species is restricted since they are strongly adsorbed. Therefore, the diffusion of EC is only possible through the vacant sites, or through swap events with final products such as Li_2EDC and Li_2BDC. In our work, the diffusion coefficient of EC was set to be ($D_{\mathrm{EC\_SEI}} = 10^{-13}\ m^2s^{-1}$) lower than the bulk value and similar to the value of electrolyte species diffusing inside the SEI[25,56]. All the physical parameters used are shown in Table S3.

The variation of concentration of species with time when reactions occur over Li_2CO_3 (001) is shown in Figure 4f. We notice that reactions over Li_2CO_3 (001) are slower than in isolation: all Li^0 are consumed in ≈ 1.2 milliseconds (ms) which is three orders of magnitude slower than the time observed in the gas-phase in isolation (0.6 μs). This is because Li_2CO_3 (001) increases the barrier of the cLi-EC• ring-opening reaction (from 23 to 53 kJ/mol, see Figure 2) slowing down the decomposition reactions, explaining the abundance of the cLi-EC• in Figure 4f compared to Figure 4b. In addition, Li^0 is less accessible to the reaction intermediates since it needs to diffuse through the Li_2CO_3 prior to any subsequent reaction. This gives more time for oLi-EC• molecules to react to form Li_2BDC before a new attack by Li^0 may occur. Hence, we notice a higher consumption of EC and more generation of organic species as compared to the case in the gas-phase in isolation. However, and like the results obtained in gas phase in isolation, the relative high energy barrier of the ethylene dissociation reaction (E_{bII} in Figure 2) explains the zero concentration of Li_2EDC. This also explains why most of the Li_2CO_3 forms through R_{III} rather than R_{VI}.

The increase in the formation of the organic species leads to a more structured multilayer SEI. The specific mass density profile along the Z-axis after 1.2 ms obtained over Li_2CO_3 (001) is shown in Figure 4g and the corresponding configuration of the simulation box in Figure 4h. Additional intermediate snapshots of the kMC simulations are added in the supporting information. A thin and dense inorganic layer (≈ 2 nm) is composed of Li_2CO_3 (which has an initial thickness of 0.88 nm at the beginning of the simulation) close to the Li-metal anode. A thick porous organic layer (≈ 17 nm) is found above (from Z-axis=2 nm to 19 nm) where the total density is mostly composed of the organic species Li_2BDC rather than EC as reported in the literature[2,7,8,11,59]. The existence of the organic layer over Li_2CO_3 layer was detected experimentally through XPS studies[12]. It should be noted that these XPS studies can demonstrate the presence of alkyl carbonates, but they are unable to differentiate between Li_2EDC and Li_2BDC[9,10,12,59]. It should be noted that the relative position of species inside the simulation box (e.g., the initial Li_2CO_3 in Figure 4e) is not fixed. Consequently, the initial number of Li_2CO_3 and the newly formed ones can slightly move through different events (diffusive or reactions), and, in particular, they can swap their position with Li^0. Figures 4f and 4g show the presence of the Li_2CO_3 layer at the beginning and at the end of the simulations respectively. The thickness of the layer slightly increases from 0.88 nm to around 2 nm, but its relative position inside the simulation box has changed due to diffusion.

The observed thickness of both the inorganic and organic layers ($\varepsilon_{\mathrm{Inorganic}}$ and $\varepsilon_{\mathrm{Organic}}$ respectively) of the SEI obtained by the analysis of the concentration profiles as a function of the z position (similar to Figure 4g) at different simulation times are shown in Figure 5. We see a linear growth of the SEI layer ($\varepsilon_{\mathrm{SEI}} = \varepsilon_{\mathrm{Inorganic}} + \varepsilon_{\mathrm{Organic}}$) with time. The linear time dependence of the long-term SEI growth with time has been reported in the literature[26]. We also notice that the growth of the inorganic layer is slower than that of the organic one since a larger amount of Li_2CO_3 is needed per one dense inorganic layer in comparison to the amount of alkyl carbonate needed to form one porous organic layer. The final thickness of the inorganic layer at the final steady state conditions of our simulations is $\approx$ 2 nm [1,2,7,8] while the thickness of the organic layer is $\approx$ 17 nm. It should be noted that, the initial number of layers of Li_2CO_3 in the setup in Figure 4e represents 0.88 nm of the final thickness of the inorganic layer. The effect of the initial number of layers of Li_2CO_3 on the concentration profile of species with time was found to be negligible, see Figure S7 for more details.

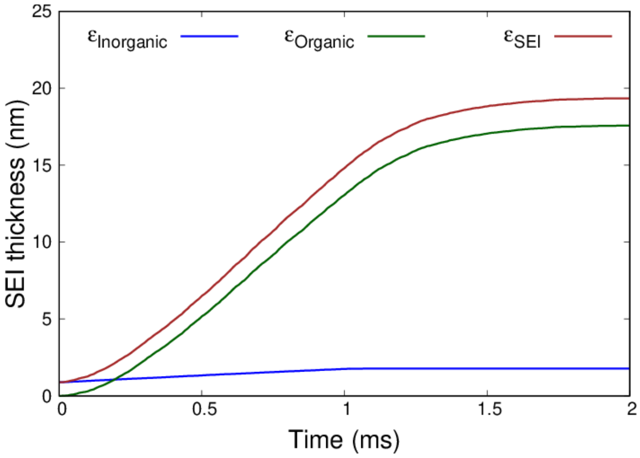

Figure 5: Evolution of the SEI layer thickness with time after EC decomposition reaction over Li_2CO_3 (001).

Some studies predict the formation of a compact organic layer due to the formation of polymers inside the organic layer of the SEI from solvent/additives degradation and polymerization[1,7,22,60]. Under these conditions, one would expect that the organic species will not freely move inside a polymeric network. Hence, we tested the effect of this polymeric environment on the setup in Figure 4e assuming a strong slowing down of the mobility of the product species. In this case, our hypothetical system consists of a kMC simulation where once an organic species (Li_2BDC or Li_2EDC) is formed, it remains captured at its position (i.e., the species are not allowed to diffuse). We found that this hypothetical setup led to a small increase in the concentration of Li_2CO_3 and the formation of a more compact organic layer which is still thicker than the inorganic layer formed. However, this setup did not fundamentally change the overall behavior of the concentration profiles with time (see Figure S8 for more details).

EC Decomposition Reactions over Li_2O (111)

Li_2O was detected inside the SEI, and it is generally assumed to originate from the decomposition of Li_2CO_3[1,7,8,61,62]. For example, Han et al. found that at high Li^0 concentration close to the vicinity of the anode (Li-metal) Li_2CO_3 is converted to Li_2O[61]. The formation and presence of CO_2 due to the electrochemical decomposition of Li_2CO_3 were also reported[62]. Hence, we tested the decomposition reactions over the most stable surface orientation of Li_2O (111). To simplify our kMC simulations, Li_2CO_3 is set to immediately decompose (barrierless reaction) to Li_2O and CO_2 (modifying R_{III} and R_{VI}), see Eq. (6).

$$Li_2CO_3 \rightarrow Li_2O + CO_2 \tag{6}$$

The energy barriers calculated using DFT over Li_2O (111) are shown in the supporting information. In contrast to the energy barriers calculated in the gas-phase in isolation, Li_2O (111) limits the ring-opening reaction R_I (E_b increases from 23 to 42 kJ/mol) and Li_2BDC formation reaction R_{IV} (from barrierless to E_b = 53 kJ/mol) but catalyzes the ethylene dissociation reaction R_{II} (E_b decreases from 65 to 48 kJ/mol) while the other reactions remain barrierless. More details about energy barriers, reaction energies and geometries of species over Li_2O (111) are found in the supporting information. We used the same kMC setup as that for Li_2CO_3 (001) but changing 4 layers of Li_2CO_3 to Li_2O and the diffusion coefficient of Li^0 in Li_2O was set to be 10^{-16} m^2s^{-1} similar to values in the literature for Li^0 diffusion in the bulk Li_2O[38,63]. When carrying out reactions over Li_2O (111), we notice that similar to Li_2CO_3 (001), the timescale for the total consumption of Li^0 was three orders of magnitude lower than in isolation, see Figure S10 for details. We form mostly the inorganic species Li_2O and some Li_2EDC but almost no Li_2BDC. The effect of carrying reactions over Li_2O (111) could explain the abundance of Li_2EDC in comparison to Li_2BDC in some experimental studies[2,7,8,11]. Overall, Li_2O (111) provides a path for the enhanced formation of Li_2EDC with respect to Li_2BDC.

In summary, our kMC results predict that if the inorganic layer is composed of Li_2CO_3, the organic layer would consist mostly of Li_2BDC, while if the inorganic layer is composed of Li_2O we would favor Li_2EDC over Li_2BDC. Thus, each surface features a specific selectivity regarding the production of the SEI organic species. This inorganic-surface specific formation of the organic layer might explain the complex, heterogenous composition of the SEI.

Relative Capacity and Calendar Aging

Calendar aging experiments are usually performed at higher temperatures to speed up the aging process, because at room temperatures it could take years to reach 80% or 90% of the initial capacity. It should be noted that the experimental time observed for capacity loss is different for different battery-aging studies even when experiments are performed using the same solvent, salts, and aging temperature[5,28,36,37]. A direct comparison of the calculated relative capacity with experimental ones is difficult as these notably depend on the many variables like electrolyte decomposition, state of charge and battery design. Hence, it is arduous to obtain a generalized experimental capacity loss plot. While our model resembles to a Li-metal anode, most calendar aging studies in the literature focus on LIBs with lithiated graphite anode. These studies report different decays for the capacity loss induced by SEI growth with time [4,37]: square root[64], linear[3,26,65,66] or combinations of both[67,68]. However, recent theoretical and experimental aging studies reported a shift from a non-linear to a final linear behavior for the capacity loss[3,5,26].

The relative capacity, as calculated according to Eq. (7), induced by SEI growth following our model is shown in Figure 6, where $\left[\mathrm{Li}^0_{\mathrm{initial}}\right]$ and $\left[\mathrm{Li}^0_{\mathrm{reacted}}\right]$ are the initial and consumed Li^0 concentrations respectively.

$$\text{Relative Capacity } \% = \frac{\left[\mathrm{Li}^0_{\mathrm{initial}}\right] - \left[\mathrm{Li}^0_{\mathrm{reacted}}\right]}{\left[\mathrm{Li}^0_{\mathrm{initial}}\right]} * 100\% \qquad (7)$$

Since the loss in capacity in isolation (absence of the inorganic surface) is much faster (microseconds) than over the inorganic surfaces (milliseconds), we have, in order to ease the comparison, normalized time (τ) from 0 to 1, representing 100 % and 0 % relative capacity, respectively.

Note that the evolution time of the relative capacity is strongly correlated to the Li^0 loss during time through Eq. (7). We observe in Figure 4b in the case of the gas-phase in isolation that the consumption of Li^0 follows a non-linear behavior. Hence, the corresponding relative capacity also follows a non-linear behavior with time as seen in Figure 6. This non-linear dependency can notably be attributed to the limited diffusion of EC and Li^0, since once the SEI starts to form Li^0 and EC are not anymore in direct contact. On the other hand, once the dense inorganic layer (Li_2CO_3) forms, electrolyte degradation reactions take place over Li_2CO_3 and results in a linear consumption of Li^0 (and relative capacity) with time, as can be seen in Figure 4f and Figure 6, respectively.

In summary, even though we used Li-metal anode in our study, rather than lithiated graphite as the anode and considered EC as the only solvent molecule, our model predicts a shift from an initial fast non-linear (in isolation) to a slower and linear (over Li_2CO_3) decay of the relative capacity. It should be noted that various mechanisms like electron migration and mechanical effect (SEI fracture and regrowth) were proposed to explain the final linear behavior for capacity loss induced by SEI growth. Our approach suggests that this linear behavior could be attributed to the effect of the inorganic layer that slows down the decomposition reactions (Li_2CO_3 can be considered as a protective layer). Moreover, this slow of Li^0 loss observed by Li_2CO_3 (001) is in line with the use of carbonate-based solvents (EC) to build a stable passivating SEI layer to protect LIBs[1,7].

In order to validate that the linear loss in Li^0 is due to the inclusion of reaction over Li_2CO_3 (001) and not a simple consequence of the preformed Li_2CO_3 layers introduced in the initial setup of our simulations as shown in Figure 4e, we used the energy barriers obtained in the gas-phase in isolation for the same initial setup as for the reactions over the Li_2CO_3 (001) i.e., with preformed Li_2CO_3 layers. We obtained the same non-linear behavior limited by diffusion as in the case where no initial Li_2CO_3 layers are used. We also mostly formed Li_2CO_3 and almost no organic species, see Figure S11 for details.

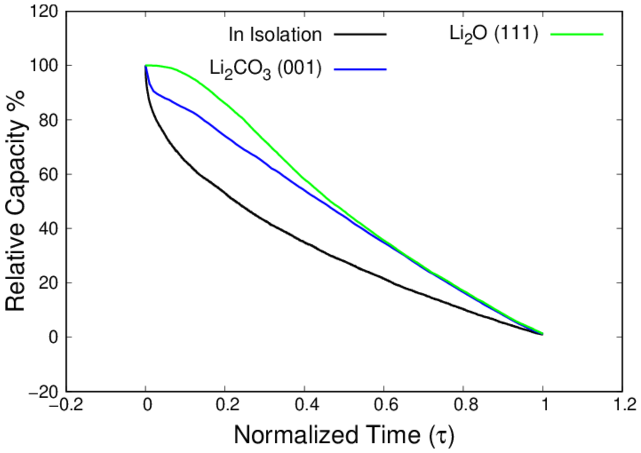

Figure 6: The behavior of the relative capacity induced by SEI growth as a function of time. The black, blue, and green lines represent the relative capacity for the loss of Li for our calculation in isolation, over Li_2CO_3 (001) and over Li_2O (111) respectively. $\tau = \frac{t}{t_{\approx 0\% \text{ of relative capacity}}}$ where t is the the theoretical (simulated) time.

For the case where EC decomposition reactions were performed over Li_2O (111), the relative capacity induced by SEI growth follows an intermediate behavior between non-linear and linear behaviors as can be seen in Figure 6. The slow diffusion of Li^0 in the bulk Li_2O explains the slow non-liner capacity loss at the initial time that shifts to linear once Li^0 meet EC over Li_2O. It is important to mention that, on one hand, the Li^0 diffusion in the bulk of Li_2O (10^{-16} m^2s^{-1}) is two orders of magnitude lower than through Li_2CO_3 (10^{-14} m^2s^{-1}). On the other hand, the ring-opening energy barrier R_I (E_{bI}= 42 kJ/mol) is lower than the value obtained over Li_2CO_3 (001) (E_{bI}= 53 kJ/mol). Consequently, Li^0 diffusion through Li_2O (111) plays a more dominant role to govern the SEI growth kinetics than over Li_2CO_3 (001). On the other hand, Li_2CO_3 (001)

stabilize the cLi-EC• slowing the decomposition reactions where the kinetics is governed by the ring-opening reaction (R_I) rather than diffusion explaining the linear loss of Li^0/capacity. A plausible way to get the SEI structure is the formation of Li_2O close to the Li-metal anode. As we get away from Li-metal, Li^0 concentration decreases and the reaction proposed in Eq. (6) becomes less probable leading to the formation of Li_2CO_3, followed by the formation of alkyl carbonates (Li-metal/Li_2O/Li_2CO_3/alkyl-carbonate/electrolyte) as suggested in the literature[12]. In any case, overall, the kMC results observed in our work are compatible with this general picture.

4. Conclusion

The solid electrolyte interphase (SEI) layer forms from the reduction of ethylene carbonate (EC) by lithium radical (Li^0) at the anode/electrolyte interface. The growth of the SEI importantly contributes to the battery-aging process which leads to capacity loss and eventually the death of the battery. In our work, we modeled the battery at storage conditions (calendar aging). We performed DFT calculations to calculate the energy barriers for EC decomposition reactions in the gas-phase in isolation and over the inorganic surfaces most likely found inside the SEI. The main contribution of this theoretical work, coupling DFT and kMC simulations, is to highlight the effect of the inorganic layer on these decomposition reactions. We used our DFT values alongside diffusion coefficients obtained from the literature to study the formation and the growth of the SEI over time by means of kinetic Monte Carlo (kMC) simulations. Our model predicts that EC decomposition reactions in isolation mostly lead to the formation of inorganic species Li_2CO_3 and a non-linear loss of Li^0/capacity. Reactions occurring over Li_2CO_3 (001) led to the formation of more organic species (dilithium butylene dicarbonate, Li_2BDC) and a more realistic SEI multilayered structure, where inorganic species are close to the anode and organic species are formed close to the interface with the electrolyte. Our simulations predict that the growth of the inorganic layer is slower compared to the growth of the organic layer. We also tested the effect of carrying reactions over Li_2O (111) based on the assumption that once Li_2CO_3 forms, it converts to Li_2O and CO_2. We found that Li_2O mostly forms inorganic species Li_2O and some Li_2EDC (dilithium ethylene dicarbonate) but few Li_2BDC. The enhanced formation of Li_2EDC over Li_2O (111) compared to Li_2BDC could explain its abundance in the organic layer in some experimental studies[2,7,8,11]. In summary, we provide evidence that reactions over Li_2CO_3 (001) or Li_2O (111) leads to contrasting selectivities in terms of the produced organic species.

The loss of Li^0/capacity over Li_2CO_3 (001) is found to have a linear behavior with time which is slower than the one observed in the case of the gas-phase in isolation, since Li_2CO_3 (001) stabilizes the radicals and increases the energy barrier for the ring-opening reactions. This slow behavior of Li^0/capacity loss over Li_2CO_3(001) could explain the common use of carbonate-based solvents to protect and extend the lifetime of LIBs[1,7]. Overall, our model predicts a shift for the loss of Li^0/capacity with time from a non-linear initial behavior in isolation limited by diffusion to a slower linear behavior (once reaction takes place over Li_2CO_3 (001)). This shift in time dependence has been observed in some experimental and theoretical works in the literature for lithiated graphite-based batteries. We also determined the relative capacity with time over Li_2O (111) and found that it follows an intermediate regime between non-linear and linear. Our work shows that considering the role of inorganic species like Li_2CO_3 and Li_2O in studying decomposition reactions leading to battery-aging could explain the kinetics, structure, and heterogeneity of the SEI.

ASSOCIATED CONTENT

The Supporting Information is available free of charge on the ACS Publication website at DOI:

Further information is available on the methodology, reaction rate constants, mean square displacement to calculate diffusion coefficients, performance tests, geometries of molecules over Li_2CO_3 (001) and Li_2O (111), EC decomposition reactions over Li_2O (111), effect of polymeric environments, typical SPPARKS input file, code modifications and additional results (PDF).

The geometries of the transition states and their corresponding reactants can be found on nomad-lab.eu under the DOI: 10.17172/NOMAD/2022.09.23-1.

Notes

The authors declare no competing financial interest.

ACKNOWLEDGEMENT

The authors would like to thank Gentien THORNER for his contribution to the fruitful discussion in developing the manuscript.

REFERENCES

(1) Philippe, B. *Insights in Li-ion Battery Interfaces through Photoelectron Spectroscopy Depth Profiling*; Digital Comprehensive Summaries of Uppsala Dissertations from the Faculty of Science and Technology, Vol. 1041; Acta Universitatis Upsaliensis, 2013.

(2) Franco, A. A. Multiscale Modelling and Numerical Simulation of Rechargeable Lithium Ion Batteries: Concepts, Methods and Challenges. *RSC Adv.* **2013**, *3*, 13027. https://doi.org/10.1039/C3RA23502E

(3) Krupp, A.; Beckmann, R.; Diekmann, T.; Ferg, E.; Schuldt, F.; Agert, C. Calendar Aging Model for Lithium-Ion Batteries Considering the Influence of Cell Characterization. *J. Energy Storage* **2022**, *45*, 103506. https://doi.org/10.1016/j.est.2021.103506

(4) Dubarry, M.; Qin, N.; Brooker, P. Calendar Aging of Commercial Li-Ion Cells of Different Chemistries – A Review. *Curr. Opin. Electrochem* **2018**, *9*, 106–113. https://doi.org/10.1016/j.coelec.2018.05.023

(5) Lewerenz, M.; Fuchs, G.; Becker, L.; Sauer, D. U. Irreversible Calendar Aging and Quantification of the Reversible Capacity Loss Caused by Anode Overhang. *J. Energy Storage* **2018**, *18*, 149–159. https://doi.org/10.1016/j.est.2018.04.029

(6) Edge, J. S.; O'Kane, S.; Prosser, R.; Kirkaldy, N. D.; Patel, A. N.; Hales, A.; Ghosh, A.; Ai, W.; Chen, J.; Yang, J.; Li, S.; Pang, M.-C.; Bravo Diaz, L.; Tomaszewska, A.; Marzook, M. W.; Radhakrishnan, K. N.; Wang, H.; Patel, Y.; Wu, B.; Offer, G. J. Lithium Ion Battery Degradation: What You Need to Know. *Phys.Chem. Chem. Phys.: PCCP* **2021**, *23*, 8200–8221. https://doi.org/10.1039/D1CP00359C

(7) Wang, A.; Kadam, S.; Li, H.; Shi, S.; Qi, Y. Review on Modeling of the Anode Solid Electrolyte Interphase (SEI) for Lithium-Ion Batteries. *npj Comput Mater* **2018**, *4*, 15. https://doi.org/10.1038/s41524-018-0064-0

(8) Franco, A. A.; Rucci, A.; Brandell, D.; Frayret, C.; Gaberscek, M.; Jankowski, P.; Johansson, P. Boosting Rechargeable Batteries R&D by Multiscale Modeling: Myth or Reality? *Chemical reviews* **2019**, *119*, 4569–4627. https://doi.org/10.1021/acs.chemrev.8b00239

(9) Gauthier, N.; Courrèges, C.; Demeaux, J.; Tessier, C.; Martinez, H. Probing the In-Depth Distribution of Organic/Inorganic Molecular Species Within the SEI of LTO/NMC and LTO/LMO Batteries: A Complementary ToF-SIMS and XPS Study. *Appl. Surf. Sci.* **2020**, *501*, 144266. https://doi.org/10.1016/j.apsusc.2019.144266

(10) R. Dedryvère; S. Laruelle; S. Grugeon; L. Gireaud; J.-M. Tarascon; D. Gonbeau. XPS Identification of the Organic and Inorganic Components of the Electrode/Electrolyte Interface Formed on a Metallic Cathode. *J. Electrochem. Soc.* **2005**, *152*, A689. https://doi.org/10.1149/1.1861994

(11) Michan, A. L.; Leskes, M.; Grey, C. P. Voltage Dependent Solid Electrolyte Interphase Formation in Silicon Electrodes: Monitoring the Formation of Organic Decomposition Products. *Chem. Mater.* **2016**, *28*, 385–398. https://doi.org/10.1021/acs.chemmater.5b04408

(12) Niehoff, P.; Passerini, S.; Winter, M. Interface Investigations of a Commercial Lithium Ion Battery Graphite Anode Material by Sputter Depth Profile X-ray Photoelectron Spectroscopy. *Langmuir* **2013**, *29*, 5806–5816. https://doi.org/10.1021/la400764r

(13) Wang, Y.; Nakamura, S.; Ue, M.; Balbuena, P. B. Theoretical Studies to Understand Surface Chemistry on Carbon Anodes for Lithium-Ion Batteries: Reduction Mechanisms of

Ethylene Carbonate. *J. Am. Chem. Soc.* **2001**, *123*, 11708–11718. https://doi.org/10.1021/ja0164529

(14) Zhang, J.; Yang, J.; Yang, L.; Lu, H.; Liu, H.; Zheng, B. Exploring the Redox Decomposition of Ethylene Carbonate–Propylene Carbonate in Li-Ion Batteries. *Mater. Adv.* **2021**, *2*, 1747–1751. https://doi.org/10.1039/D0MA00847H

(15) Abbott, J. W.; Hanke, F. Kinetically Corrected Monte Carlo-Molecular Dynamics Simulations of Solid Electrolyte Interphase Growth. *J. Chem. Theory Comput.* **2022**, *18*, 925–934. https://doi.org/10.1021/acs.jctc.1c00921

(16) Yang, P.-Y.; Pao, C.-W. Molecular Simulations of the Microstructure Evolution of Solid Electrolyte Interphase during Cyclic Charging/Discharging. *ACS Appl. Mater. Interfaces* **2021**, *13*, 5017–5027. https://doi.org/10.1021/acsami.0c18783 .

(17) Spotte-Smith, E. W. C.; Kam, R. L.; Barter, D.; Xie, X.; Hou, T.; Dwaraknath, S.; Blau, S. M.; Persson, K. A. Toward a Mechanistic Model of Solid–Electrolyte Interphase Formation and Evolution in Lithium-Ion Batteries. *ACS Energy Lett.* **2022**, *7*, 1446–1453. https://doi.org/10.1021/acsenergylett.2c00517

(18) Kamphaus, E. P.; Angarita-Gomez, S.; Qin, X.; Shao, M.; Engelhard, M.; Mueller, K. T.; Murugesan, V.; Balbuena, P. B. Role of Inorganic Surface Layer on Solid Electrolyte Interphase Evolution at Li-Metal Anodes. *ACS Appl. Mater. Interfaces* **2019**, *11*, 31467–31476. https://doi.org/10.1021/acsami.9b07587

(19) Kamphaus, E. P.; Gomez, S. A.; Qin, X.; Shao, M.; Balbuena, P. B. Effects of Solid Electrolyte Interphase Components on the Reduction of LiFSI over Lithium Metal. *Chemphyschem* **2020**, *21*, 1310–1317. https://doi.org/10.1002/cphc.202000174

(20) Xu, W.; Liao, X.; Xu, W.; Sun, C.; Zhao, K.; Zhao, Y.; Hu, C. Gradient SEI Layer Induced by Liquid Alloy Electrolyte Additive for High Rate Lithium Metal Battery. *Nano Energy* **2021**, *88*, 106237. https://doi.org/10.1016/j.nanoen.2021.106237

(21) Lespes, N.; Filhol, J.-S. Using Implicit Solvent in Ab Initio Electrochemical Modeling: Investigating Li^+/Li Electrochemistry at a Li/Solvent Interface. *J. Chem. Theory Comput.* **2015**, *11*, 3375–3382. https://doi.org/10.1021/acs.jctc.5b00170

(22) Kuai, D.; Balbuena, P. B. Solvent Degradation and Polymerization in the Li-Metal Battery: Organic-Phase Formation in Solid-Electrolyte Interphases. *ACS Appl. Mater. Interfaces* **2022**, *14*, 2817–2824. https://doi.org/10.1021/acsami.1c20487

(23) Single, F.; Latz, A.; Horstmann, B. Identifying the Mechanism of Continued Growth of the Solid-Electrolyte Interphase. *ChemSusChem* **2018**, *11*, 1950–1955. https://doi.org/10.1002/cssc.201800077

(24) Abada, S.; Petit, M.; Lecocq, A.; Marlair, G.; Sauvant-Moynot, V.; Huet, F. Combined Experimental and Modeling Approaches of the Thermal Runaway of Fresh and Aged Lithium-Ion Batteries. J. Power Sources **2018**, *399*, 264–273. https://doi.org/10.1016/j.jpowsour.2018.07.094

(25) Christensen, J.; Newman, J. A Mathematical Model for the Lithium-Ion Negative Electrode Solid Electrolyte Interphase. J. Electrochem. Soc. **2004**, *151*, A1977. https://doi.org/10.1149/1.1804812

(26) Kolzenberg, L. von; Latz, A.; Horstmann, B. Solid-Electrolyte Interphase During Battery Cycling: Theory of Growth Regimes. *ChemSusChem* **2020**, *13*, 3901–3910. https://doi.org/10.1002/cssc.202000867

(27) Li, D.; Danilov, D.; Zhang, Z.; Chen, H.; Yang, Y.; Notten, P. H. L. Modeling the SEI-Formation on Graphite Electrodes in LiFePO 4 Batteries. *J. Electrochem. Soc.* **2015**, *162*, A858-A869. https://doi.org/10.1149/2.0161506jes

(28) Keil, J.; Paul, N.; Baran, V.; Keil, P.; Gilles, R.; Jossen, A. Linear and Nonlinear Aging of Lithium-Ion Cells Investigated by Electrochemical Analysis and In-Situ Neutron Diffraction. *J. Electrochem. Soc.* **2019**, *166*, A3908-A3917. https://doi.org/10.1149/2.1271915jes

(29) Attia, P. M.; Das, S.; Harris, S. J.; Bazant, M. Z.; Chueh, W. C. Electrochemical Kinetics of SEI Growth on Carbon Black: Part I. Experiments. *J. Electrochem. Soc.* **2019**, *166*, E97-E106. https://doi.org/10.1149/2.0231904jes

(30) Franco, A. A.; Yin, Y. Monte Carlo Modeling of Interfacial Electrochemistry for Energy Applications. In *Encyclopedia of Interfacial Chemistry*; Elsevier, 2018; pp 739–751. https://doi.org/10.1016/B978-0-12-409547-2.13364-5

(31) Thangavel, V.; Guerrero, O. X.; Quiroga, M.; Mikala, A. M.; Rucci, A.; Franco, A. A. A Three Dimensional Kinetic Monte Carlo Model for Simulating the Carbon/Sulfur Mesostructural Evolutions of Discharging Lithium Sulfur Batteries. *Energy Storage Mater.* **2020**, *24*, 472–485. https://doi.org/10.1016/j.ensm.2019.07.011

(32) Yin, Y.; Zhao, R.; Deng, Y.; Franco, A. A. Compactness of the Lithium Peroxide Thin Film Formed in Li-O2 Batteries and Its Link to the Charge Transport Mechanism: Insights from Stochastic Simulations. *J. Phys. Chem. Lett.* **2017**, *8*, 599–604. https://doi.org/10.1021/acs.jpclett.6b02732

(33) Zhai, P.; Liu, L.; Gu, X.; Wang, T.; Gong, Y. Interface Engineering for Lithium Metal Anodes in Liquid Electrolyte. *Adv. Energy Mater.* **2020**, *10*, 2001257. https://doi.org/10.1002/aenm.202001257

(34) Single, F.; Horstmann, B.; Latz, A. Revealing SEI Morphology: In-Depth Analysis of a Modeling Approach. *J. Electrochem. Soc.* **2017**, *164*, E3132-E3145. https://doi.org/10.1149/2.0121711jes

(35) Shi, S.; Lu, P.; Liu, Z.; Qi, Y.; Hector, L. G.; Li, H.; Harris, S. J. Direct Calculation of Li-Ion Transport in the Solid Electrolyte Interphase. *J. Am. Chem. Soc.* **2012**, *134*, 15476–15487. https://doi.org/10.1021/ja305366r

(36) Hellqvist Kjell, M.; Malmgren, S.; Ciosek, K.; Behm, M.; Edström, K.; Lindbergh, G. Comparing Aging of Graphite/LiFePO 4 Cells at 22 °C and 55 °C – Electrochemical and Photoelectron Spectroscopy Studies. *J. Power Sources* **2013**, *243*, 290–298. https://doi.org/10.1016/j.jpowsour.2013.06.011

(37) Gasper, P.; Gering, K.; Dufek, E.; Smith, K. Challenging Practices of Algebraic Battery Life Models through Statistical Validation and Model Identification via Machine-Learning. *J. Electrochem. Soc.* **2021**, *168*, 20502. https://doi.org/10.1149/1945-7111/abdde1

(38) Ramasubramanian, A.; Yurkiv, V.; Foroozan, T.; Ragone, M.; Shahbazian-Yassar, R.; Mashayek, F. Lithium Diffusion Mechanism through Solid–Electrolyte Interphase in Rechargeable Lithium Batteries. *J. Phys. Chem. C* **2019**, *123*, 10237–10245. https://doi.org/10.1021/acs.jpcc.9b00436

(39) Kitz, P. G.; Lacey, M. J.; Novák, P.; Berg, E. J. Operando Investigation of the Solid Electrolyte Interphase Mechanical and Transport Properties Formed from Vinylene Carbonate and Fluoroethylene Carbonate. *J. Power Sources* **2020**, *477*, 228567. https://doi.org/10.1016/j.jpowsour.2020.228567

(40) Hayamizu, K. Temperature Dependence of Self-Diffusion Coefficients of Ions and Solvents in Ethylene Carbonate, Propylene Carbonate, and Diethyl Carbonate Single Solutions and Ethylene Carbonate + Diethyl Carbonate Binary Solutions of LiPF 6 Studied by NMR. *J. Chem. Eng. Data* **2012**, *57*, 2012–2017. https://doi.org/10.1021/je3003089

(41) Kresse, G.; Furthmüller, J. Efficient Iterative Schemes for Ab Initio Total-Energy Calculations Using a Plane-Wave Basis Set. *Phys. Rev. B* **1996**, *54*, 11169–11186. https://doi.org/10.1103/PhysRevB.54.11169

(42) Kresse, G.; Hafner, J. Ab Initio Molecular Dynamics for Liquid Metals. *Phys. Rev. B* **1993**, *47*, 558–561. https://doi.org/10.1103/PhysRevB.47.558

(43) Kresse, G.; Furthmüller, J. Efficiency of Ab-Initio Total Energy Calculations for Metals and Semiconductors Using a Plane-Wave Basis Set. *Comput. Mater. Sci.* **1996**, *6*, 15–50. https://doi.org/10.1016/0927-0256(96)00008-0

(44) Kresse, G.; Hafner, J. Ab Initio Molecular Dynamics for Open-Shell Transition Metals. *Phys. Rev. B Condens. Matter* **1993**, *48*, 13115–13118. https://doi.org/10.1103/physrevb.48.13115

(45) Perdew, J. P.; Burke, K.; Ernzerhof, M. Generalized Gradient Approximation Made Simple [Phys. Rev. Lett. 77, 3865 (1996)]. *Phys. Rev. Lett.* **1997**, *78*, 1396. https://doi.org/10.1103/PhysRevLett.78.1396

(46) Steinmann, S. N.; Corminboeuf, C. Comprehensive Benchmarking of a Density-Dependent Dispersion Correction. *J. Chem. Theory Comput.* **2011**, *7*, 3567–3577. https://doi.org/10.1021/ct200602x

(47) Steinmann, S. N.; Corminboeuf, C. A Generalized-Gradient Approximation Exchange Hole Model for Dispersion Coefficients. *J. Chem. Phys.* **2011**, *134*, 44117. https://doi.org/10.1063/1.3545985

(48) Monkhorst, H. J.; Pack, J. D. Special Points for Brillouin-Zone Integrations. *Phys. Rev. B* **1976**, *13*, 5188–5192. https://doi.org/10.1103/PhysRevB.13.5188

(49) P. Fleurat-Lessard. *Reaction path.* http://pfleurat.free.fr/ReactionPath.php (accessed 2023-04-04).

(50) Henkelman, G.; Uberuaga, B. P.; Jónsson, H. A Climbing Image Nudged Elastic Band Method for Finding Saddle Points and Minimum Energy Paths. *J. Chem. Phys.* **2000**, *113*, 9901–9904. https://doi.org/10.1063/1.1329672

(51) Henkelman, G.; Jónsson, H. A Dimer Method for Finding Saddle Points on High Dimensional Potential Surfaces Using Only First Derivatives. *J. Chem. Phys.* **1999**, *111*, 7010–7022. https://doi.org/10.1063/1.480097

(52) Bortz, A.B.; Kalos, M.H.; Lebowitz, J.L. A New Algorithm for Monte Carlo Simulation of Ising Spin Systems. *J. Comput. Phys.* **1975**, *17*, 10–18. https://doi.org/10.1016/0021-9991(75)90060-1

(53) Voter, A. Introduction to the Kinetic Monte Carlo Method. In Radiation Effects in Solids; Sickafus, K. E., Kotomin, E. A., Uberuaga, B. P., Eds.; Springer Netherlands: Dordrecht, 2007; pp 1-23. https://doi.org/10.1007/978-1-4020-5295-8_1

(54) Corbett C. Battaile. The Kinetic Monte Carlo Method: Foundation, Implementation, and Application. *Comput. Methods Appl. Mech. Eng* **2008**, *197* (41), 3386–3398. . https://doi.org/10.1016/j.cma.2008.03.010

(55) Plimpton, S.; Battaile, C.; Chandross, M.; Holm, L.; Thompson, A.; Tikare, V.; Wagner, G.; Webb, E.; Zhou, X.; Cardona, C. G.; Slepov. *SPPARKS*: *Crossing the mesoscale no-mans land via parallel kinetic Monte Carlo*. Technical Report for Sandia National Laboratories, 2009. https://www.osti.gov/biblio/966942 (accessed 2023-05-18).

(56) Liu, L.; Park, J.; Lin, X.; Sastry, A. M.; Lu, W. A Thermal-Electrochemical Model that Gives Spatial-Dependent Growth of Solid Electrolyte Interphase in a Li-Ion Battery. *J. Power Sources* **2014**, *268*, 482–490. https://doi.org/10.1016/j.jpowsour.2014.06.050

(57) Shi, S.; Qi, Y.; Li, H.; Hector, L. G. Defect Thermodynamics and Diffusion Mechanisms in Li_2CO_3 and Implications for the Solid Electrolyte Interphase in Li-Ion Batteries. *J. Phys. Chem. C* **2013**, *117* (17), 8579–8593. https://doi.org/10.1021/jp310591u

(58) Iddir, H.; Curtiss, L. A. Li Ion Diffusion Mechanisms in Bulk Monoclinic Li_2CO_3 Crystals from Density Functional Studies. *J. Phys. Chem. C* **2010**, *114* (48), 20903–20906. https://doi.org/10.1021/jp1086569

(59) Bedrov, D.; Smith, G. D.; van Duin, A. C. T. Reactions of Singly-Reduced Ethylene Carbonate in Lithium Battery Electrolytes: A Molecular Dynamics Simulation Study Using the ReaxFF. *J. Phys. Chem. A* **2012**, *116* (11), 2978–2985. https://doi.org/10.1021/jp210345b

(60) Peled, E.; Bar Tow, D.; Merson, A.; Gladkich, A.; Burstein, L.; Golodnitsky, D. Composition, Depth Profiles and Lateral Distribution of Materials in the SEI Built on HOPG-TOF SIMS and XPS Studies. *J. Power Sources* **2001**, *97-98*, 52–57. https://doi.org/10.1016/S0378-7753(01)00505-5

(61) Han, B.; Zhang, Z.; Zou, Y.; Xu, K.; Xu, G.; Wang, H.; Meng, H.; Deng, Y.; Li, J.; Gu, M. Poor Stability of Li_2CO_3 in the Solid Electrolyte Interphase of a Lithium-Metal Anode Revealed by Cryo-Electron Microscopy. *Adv. Mater.* **2021**, *33* (22), e2100404. https://doi.org/10.1002/adma.202100404

(62) Cao, D.; Tan, C.; Chen, Y. Oxidative Decomposition Mechanisms of Lithium Carbonate on Carbon Substrates in Lithium Battery Chemistries. Nat. Commun. 2022, 13 (1), 4908. https://doi.org/10.1038/s41467-022-32557-w

(63) Guan, P.; Liu, L.; Lin, X. Simulation and Experiment on Solid Electrolyte Interphase (SEI) Morphology Evolution and Lithium-Ion Diffusion. *J. Electrochem. Soc.* **2015**, *162* (9), A1798-A1808. https://doi.org/10.1149/2.0521509jes

(64) Naumann, M.; Schimpe, M.; Keil, P.; Hesse, H. C.; Jossen, A. Analysis and Modeling of Calendar Aging of a Commercial $LiFePO_4$/Graphite Cell. *J. Energy Storage* **2018**, *17*, 153–169. https://doi.org/10.1016/j.est.2018.01.019

(65) Belt, J.; Utgikar, V.; Bloom, I. Calendar and PHEV Cycle Life Aging of High-Energy, Lithium-Ion Cells Containing Blended Spinel and Layered-Oxide Cathodes. *J. Power Sources* **2011**, *196* (23), 10213–10221. https://doi.org/10.1016/j.jpowsour.2011.08.067

(66) Grolleau, S.; Delaille, A.; Gualous, H.; Gyan, P.; Revel, R.; Bernard, J.; Redondo-Iglesias, E.; Peter, J. Calendar Aging of Commercial Graphite/$LiFePO_4$ Cell – Predicting Capacity Fade Under Time Dependent Storage Conditions. *J. Power Sources* **2014**, *255*, 450–458. https://doi.org/10.1016/j.jpowsour.2013.11.098

(67) Käbitz, S.; Gerschler, J. B.; Ecker, M.; Yurdagel, Y.; Emmermacher, B.; André, D.; Mitsch, T.; Sauer, D. U. Cycle and Calendar Life Study of a Graphite $LiNi_{1/3}Mn_{1/3}Co_{1/3}O_2$ Li-Ion High Energy System. Part A: Full Cell Characterization. *J. Power Sources* **2013**, *239*, 572–583. https://doi.org/10.1016/j.jpowsour.2013.03.045

(68) Ecker, M.; Gerschler, J. B.; Vogel, J.; Käbitz, S.; Hust, F.; Dechent, P.; Sauer, D. U. Development of a Lifetime Prediction Model for Lithium-Ion Batteries Based on Extended Accelerated Aging Test Data. *J. Power Sources* **2012**, *215*, 248–257. https://doi.org/10.1016/j.jpowsour.2012.05.012

Graphical Abstract